

The star formation history of the SMC star cluster NGC 419

Stefano Rubele^{1,2}, Leandro Kerber³ and Léo Girardi¹

¹ *Osservatorio Astronomico di Padova – INAF, Vicolo dell’Osservatorio 5, I-35122 Padova, Italy*

² *Dipartimento di Astronomia, Università di Padova, Vicolo dell’Osservatorio 2, I-35122 Padova, Italy*

³ *Laboratório de Astrofísica Teórica e Observacional, Departamento de Ciências Exatas e Tecnológicas, Universidade Estadual de Santa Cruz, Rodovia Ilhéus-Itabuna, km. 16 – Ilhéus, Bahia, CEP 45662-000, Brazil*

Accepted 2009 December 10. Received 2009 December 10; in original form 2009 November 9

ABSTRACT

The rich SMC star cluster NGC 419 has recently been found to present both a broad main sequence turn-off and a dual red clump of giants, in the sharp colour–magnitude diagrams (CMD) derived from the High Resolution Channel of the Advanced Camera for Surveys on board the *Hubble Space Telescope*. In this work, we apply to the NGC 419 data the classical method of star formation history (SFH) recovery via CMD reconstruction, deriving for the first time this function for a star cluster with multiple turn-offs. The values for the cluster metallicity, reddening, distance and binary fraction, were varied within the limits allowed by present observations. The global best-fitting solution is an excellent fit to the data, reproducing all the CMD features with striking accuracy. The corresponding star formation rate is provided together with estimates of its random and systematic errors. Star formation is found to last for at least 700 Myr, and to have a marked peak at the middle of this interval, for an age of 1.5 Gyr. Our findings argue in favour of multiple star formation episodes (or continued star formation) being at the origin of the multiple main sequence turn-offs in Magellanic Cloud clusters with ages around 1 Gyr. It remains to be tested whether alternative hypotheses, such as a main sequence spread caused by rotation, could produce similarly good fits to the data.

Key words: Stars: evolution – Hertzsprung-Russell (HR) and C-M diagrams

1 INTRODUCTION

Back in the nineties, the *Hubble Space Telescope* Wide Field Planetary Camera 2 (*HST*/WFPC2) opened a new era in the study of stellar populations in the Magellanic Clouds. Starting from Gallagher et al. (1996), many authors were able to derive the detailed star formation history of LMC and SMC fields, via the analysis of deep CMDs reaching well below the oldest main sequence turn-offs (MSTO). It became possible as well the accurate measurement of the properties and structure of many populous star clusters (e.g. Mighell et al. 1996; Elson et al. 1998; Rich et al. 2000, 2001; Gouliermis et al. 2004; Kerber et al. 2007).

The higher efficiency and larger area of the Advanced Camera for Surveys (ACS) further improved the situation. One of the latest achievements in the field was the conclusive evidence, based on ACS data, that many star clusters in the LMC with ages typically larger than 1 Gyr, present double or multiple main sequence turn-offs (MMSTO; Mackey & Broby Nielsen 2007; Mackey et al. 2008;

Milone et al. 2009). This effect was, in precedence, already indicated by ground-based deep CMDs (Bertelli et al. 2003; Baume et al. 2007), which however were far from presenting the fine details of the ACS ones.

While there is firm observational basis for the presence of MMSTOs in star clusters, their interpretation is far from being settled. Once it has been demonstrated that the presence of binaries cannot mimic the detailed shape of MMSTOs (see Mackey et al. 2008; Goudfrooij et al. 2009) the most obvious interpretation is that they are the signature of stellar populations spanning several hundreds of Myr in age. This interpretation however poses a major challenge to the understanding of star formation and dynamics in star clusters, since it is not obvious how objects with relatively shallow potential wells could retain their gas and continue forming stars for so long a time. Bekki & Mackey (2009) propose a mechanism to explain the bluest MSTOs as being due to a second event of star formation driven by the collision with a giant molecular cloud; this hypothesis however does only explain *double* MSTOs and not the continuous

MMSTO structures observed by Goudfrooij et al. (2009) in NGC 1846.

Bastian & de Mink (2009) have recently advanced a completely different explanation for MMSTOs: the phenomenon could be caused by the effects of rotation during the main sequence evolution of stars. For a coeval population, the most rapid rotators would evolve to lower T_{eff} and generate the redder turn-offs. The hypothesis is certainly interesting, although it requires an ad hoc decrease of rotation velocities with the stellar mass, and relatively high rotation velocities – nearly half the critical break-up rotation rate – in order to explain the observed features. Whether these rotation velocities can be typical of A and F stars in the Magellanic Clouds, and cause the large spread in T_{eff} that is apparently observed, is yet to be clarified by new observations.

Whether the MMSTO phenomenon can be explained by stellar populations of single or multiple ages, bears very much in the interpretation of CMDs of nearby galaxies in general. In deriving SFH of galaxies, one assumes that their CMDs are made by the superposition of populations of different ages, each one presenting a narrow MSTO. Were the MSTOs of single-burst populations intrinsically broad, most works of SFH-recovery in nearby galaxies would have to be revised to some extent.

Given the above situation, we decided to test if the extended-SFH hypothesis could really explain the MMSTOs in ~ 1 -Gyr old star clusters in the Magellanic Clouds. As a first target, we choose the rich SMC star cluster NGC 419. Two aspects make this cluster an ideal target for our goals. First, it does not only present a MMSTO (Glatt et al. 2008) but also has a dual clump of red giants (Girardi et al. 2009a), which is the signature of stars close to the transition between those that form an electron-degenerate core after H-exhaustion, and those that do not. This additional fine structure of the CMD provides strong constraints to the cluster mean age and to the efficiency of convective core overshooting in stars (Girardi et al. 2009a), probably helping to limit the family of stellar models that can be fit in the process of SFH-recovery. Second, the central region of NGC 419 counts with extremely accurate photometry provided by the High Resolution Channel (HRC) of ACS. As a bonus, the field contamination is almost negligible for this cluster.

This paper is structured as follows: Sect. 2 briefly describes the SFH-recovery method and its application to the NGC 419 data. Sect. 3 presents the results for NGC 419 and a discussion about the random and systematic errors in the recovered SFH, due to the statistical fluctuations and uncertainties in reddening, distance, metallicity, binary fraction, and field contamination. Sect. 4 draws the final conclusions.

2 PREPARING NGC 419 FOR SFH-RECOVERY

2.1 Data and photometry

The dataset used in this paper has been retrieved from the HST archive (GO-10396, PI: J.S. Gallagher) and consists of a 740 arcsec^2 area centered on NGC 419, observed with the ACS/HRC in the filters F555W and F814W. The same

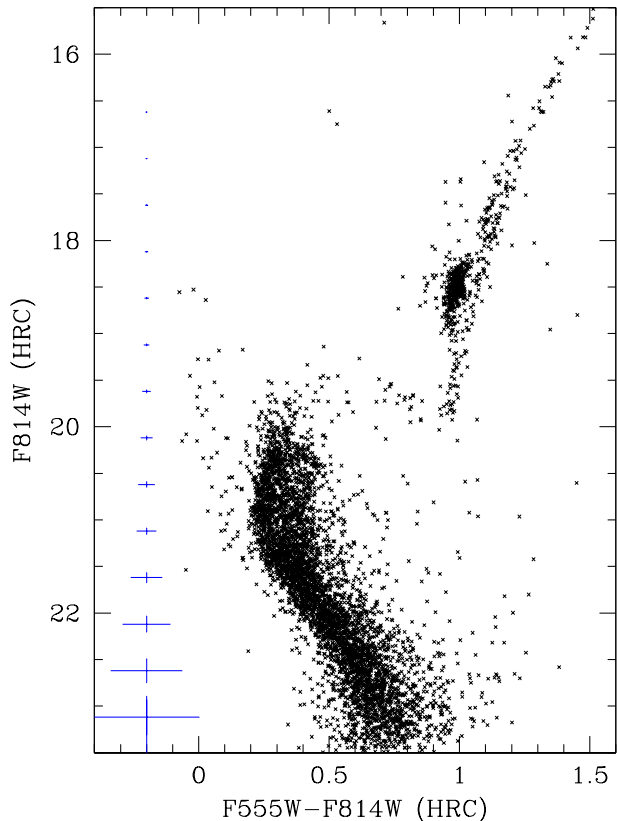


Figure 1. The CMD for NGC 419 as derived from the HRC data centered on the cluster, after the re-reduction described in this paper and without applying any quality cut to the photometry. The 1σ error bars, as derived from artificial star tests (see Sect. 2.2), are drawn at the left.

images have already been analysed by Glatt et al. (2008, 2009) and Girardi et al. (2009a). Girardi et al. (2009b, its figure 1) provide a false-color version of these HRC images, together with a comparison with the much wider ACS Wide Field Channel (WFC) images of the same cluster. There, one may notice that the HRC field samples just the very inner part of the cluster, and that the distribution of stars over its area is quite uniform.

The original data has been re-reduced as described in Girardi et al. (2009a). Essentially, we have accessed the archival images already processed and calibrated using the standard procedures mentioned in Sirianni et al. (2005). Aperture and Point Spread Function (PSF) photometry with the DAOPHOT package (Stetson 1987) were performed within a 2 pix radius, and aperture corrections were applied. The resulting CMDs are very similar to those described in Glatt et al. (2008). The PSF photometry was then preferred and used for all subsequent applications.

Fig. 1 shows the ACS/HRC data for NGC 419, in the F814W vs. F555W – F814W CMD. This plot will be used as a reference to our analysis.

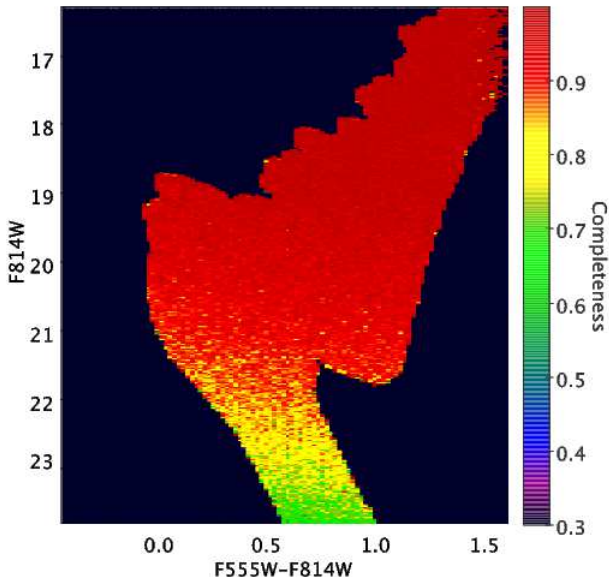


Figure 2. Completeness map, derived from the complete set of ASTs.

2.2 Assessing photometric errors and completeness

In order to characterize the errors in the photometry and the completeness of the sample, we have performed a series of artificial star tests (AST) on the reduced images (see e.g. Gallart et al. 1999; Harris & Zaritsky 2001). The procedure consists of adding stars of known magnitude and colour at random places in the F555W and F814W images, and redoing the photometry exactly in the same way as before. The artificial stars are then searched in the photometric catalogues, and when recovered the changes in their magnitudes are stored for subsequent use.

In order to avoid the introduction of additional crowding in the images, artificial stars are positioned at distances much higher than their PSF width. We found that the PSF radius in our ACS/HRC images is of $\lesssim 7$ pix, whereas our fitting radius is of 2 pix. So, our AST are distributed on a grid spaced by 20 pix, which is each time randomly displaced over the image.

A total of 3.4×10^9 ASTs were performed, covering in an almost uniform way the CMD area of the observed stars as well as the area for which we build the “partial models” to be used in the SFH analysis (see Sect. 2.3 below). Then, the ratio between recovered and input stars gives origin to the completeness map of Fig. 2. Note that the 90 % completeness limit is located at $F814W \sim 21.7$, which is well below the position of the MMSTOs in NGC 419.

Another important aspect is that the stellar density is quite constant over the HRC images, as well as the completeness. For instance, at magnitudes 22.15, from the image center to the borders the completeness changes from 0.87 to 0.90 for the F555W filter, and from 0.78 to 0.85 for F814W. Since this difference is very small and the bottom part of the CMD will not be used in our analysis, we do not apply any position-dependent completeness to the CMDs, but simply the average values derived from all the ASTs.

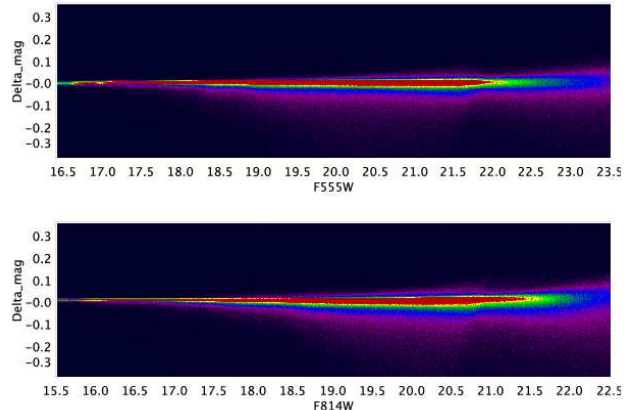


Figure 3. Map of photometric errors as a function of input F555W and F814W, as derived from the ASTs. The errors are defined as the difference between the recovered and input magnitudes.

Figure 3 presents the differences between the recovered and input magnitudes of ASTs, as a function of their input magnitudes. These differences give a good handle of the photometric errors effectively present in the data. The error distributions are slightly asymmetric because of crowding.

2.3 The partial models

The basic process of SFH-recovery is the decomposition of an observed CMD as the sum of several “partial models”, which represent stellar populations in very limited intervals of age and metallicity. In our case we will assume a constant age-metallicity relation (AMR) i.e., a single value for the metallicity for all ages, since so far there are no evidences for significant spreads in metallicity in star clusters like NGC 419 (e.g. Mucciarelli et al. 2008). Hence, each partial model is defined as a stellar aggregate with constant star formation over an age interval of width $\Delta \log t = 0.05$ dex. This is a fine age resolution for a work of SFH-recovery; suffice it to recall that the age bins adopted in the SFH-recovery of nearby galaxies are usually wider than 0.1 dex in $\log t$ (see e.g. Gallart et al. 1999; Harris & Zaritsky 2001; Dolphin et al. 2003, for some examples). The age interval covered by our partial models goes from $\log(t/\text{yr}) = 8.9$ to 9.4, which is much wider than the interval suggested by the position of NGC 419 MMSTOs. So, for each set of parameters, we have a total of 10 partial models, completely encompassing the age interval of interest.

The other parameters defining a set of partial models are the V -band extinction A_V , the distance modulus $(m-M)_0$, the metallicity $[\text{Fe}/\text{H}]$, and the binary fraction f_b ; these will be varied in our analysis as described below. Other parameters describe the area of the CMD to be sampled, and its resolution. With basis on our Figs. 1 and 2, we decide to limit the CMD area to be analysed as: $F555W - F814W$ between -0.4 and 1.6 , and $F814W$ between 16.32 and 22.0 . Within these limits, stars are not saturated, and completeness is above 80 %. The CMD resolution is set to be 0.02 mag both in colour and in magnitude.

The partial models are simulated with the aid of the stellar population synthesis tool TRILEGAL (Girardi et al.

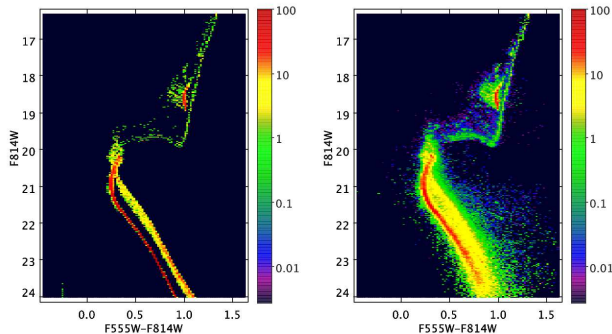


Figure 4. Hess diagram for a single partial model, before (left panel) and after (right panel) applying the results of ASTs. The partial model has a mean age $\log(t/\text{yr}) = 9.125$, metallicity $[\text{Fe}/\text{H}] = -0.95$, and binary fraction $f_b = 0.18$. The colour scale indicates the density of stars.

2005) in its version 1.3, which stands on the Marigo et al. (2008) isochrones, transformed to the ACS/HRC Vegamag photometry using Girardi et al. (2008) bolometric corrections and extinction coefficients. The IMF was assumed to be the Chabrier (2001) lognormal one. The output catalogues from TRILEGAL are first degraded applying the results from the ASTs – which results in the blurring and depopulation of the bottom part of the CMDs – and then converted into Hess diagrams. Fig. 4 illustrates one of such diagrams for a partial model before and after the results of ASTs have been applied.

2.4 The range of cluster parameters

In our analysis, we have tried to cover the complete possible range of parameters for NGC 419, in particular:

Distance modulus $(m-M)_0$: Our reference value for the SMC distance modulus is $(m-M)_0 = 18.89 \pm 0.14$ (Harries et al. 2003), which is a value very similar to many other recent determinations (e.g. Crowl et al. 2001; Lah et al. 2005; North et al. 2009). In practice, however, we explored $(m-M)_0$ values between 18.75 and 18.97.

Extinction A_V : The Schlegel et al. (1998) extinction maps provide $E_{B-V} = 0.10 \pm 0.01$ for an area of radius equal to $5'$ around NGC 419, which translates into $A_V = 0.32 \pm 0.03$. A similar search in the maps from Zaritsky et al. (2002), with a $12'$ radius, produces $A_V = 0.27 \pm 0.28$. In practice, we explored A_V values between 0.12 and 0.38.

Metallicity $[\text{Fe}/\text{H}]$: Works based on isochrone fitting (e.g. Durand et al. 1984) as well as Ca II triplet observations (Kayser et al. 2009) have suggested $[\text{Fe}/\text{H}]$ values similar to -0.7 ± 0.3 for NGC 419. Interestingly, the metal abundances of other SMC clusters with similar ages are uncertain as well. Suffices it to mention the recent AMR for the SMC as derived from Parisi et al. (2009, their figure 14), which shows SMC clusters with ages smaller than 2 Gyr covering the complete $[\text{Fe}/\text{H}]$ interval between -0.5 and -1.1 . The situation is far from clear and high resolution spectroscopy of a handful of giants in 1-Gyr old SMC clusters is definitely

needed. In this work, we have decided to explore the whole $-0.5 < [\text{Fe}/\text{H}] < -1.1$ interval.

Binary fraction f_b : Elson et al. (1998), using the shape of the main sequence in a deep CMD (obtained with HST) for the LMC cluster NGC 1818, determined a binary fraction from ~ 0.20 to ~ 0.35 , from the center to the outer parts of the cluster. These binary fractions refer only to the binaries with high primary/secondary mass ratio, say of above 0.7, because these are the only ones which separate clearly from the single-star main sequence in CMDs. In our previous work on NGC 419 (Girardi et al. 2009a), we have already noticed that the HRC CMD was indicating a binary fraction of the order of 0.2, consistent with the central region of NGC 1818. In the following, we will adopt a reference value of $f_b \sim 0.18$; notice however that we have explored f_b values from 0.10 to 0.28. The distribution of primary/secondary mass ratios is assumed to be uniform over the interval from 0.7 to 1.0

Compared to the other parameters, the binary fraction is the less important in defining the quality of a CMD fit, as will be illustrated below. A clear advantage of exploring ranges for the other parameters – instead of taking single values from the literature – is that in this way we can partially compensate for the possible errors and offsets in the theoretical models: Errors in the zeropoints of bolometric corrections and on the helium content of stellar models could be easily compensated by a change in apparent distance modulus $(m-M)_0 + A_V$. Errors in the theoretical T_{eff} -color relations can also be compensated by small changes in both A_V and $[\text{Fe}/\text{H}]$. Therefore, the final best-fitting values for these quantities are to be associated to the stellar models which we are using. Different sets of stellar models are likely to produce slightly different best-fitting values.

3 RECOVERING THE STAR FORMATION HISTORY

3.1 Method

To recover the SFH of NGC 419, we use an adapted version of the pipeline that is being built to analyse data from the VISTA survey of the Magellanic Clouds (VMC; see Cioni et al. 2008). The method is fully described, and tested on VMC simulated data by Kerber et al. (2009). In brief, after building the Hess diagram for the data and partial models, the StarFISH code (Harris & Zaritsky 2001, 2004) is used to find the linear combination of partial models that minimizes a χ^2 -like statistic as defined in Dolphin (2002). The solution is characterized by the minimum χ^2 , χ^2_{min} , and by a set of partial model coefficients corresponding to the several age bins. These latter translate directly in the star formation rate as function of age, $\text{SFR}(t)$.

The SFH-recovery is repeated for each of the $(m-M)_0$, A_V , $[\text{Fe}/\text{H}]$, and f_b values. In order to limit the space of parameters to be covered, the procedure is essentially the following: for a given value of $[\text{Fe}/\text{H}]$ and f_b , we cover a significant region of the $(m-M)_0$ versus A_V plane, performing SFH-recovery for each point in a grid, and then building a map of the χ^2_{min} for the solutions. Examples of these maps are presented in Fig. 5. The maps are extended so that the

minimum χ_{\min}^2 for a given value of $[\text{Fe}/\text{H}]$ can be clearly identified, as well as the regions in which χ_{\min}^2 increases by a factor of about 1.5. The typical resolution of such maps is of 0.01 in $(m-M)_0$ and 0.005 in A_V .

The procedure is done for several values of $[\text{Fe}/\text{H}]$. χ_{\min}^2 maps for different $[\text{Fe}/\text{H}]$ present relative minima in slightly different positions, so that the final resulting maps do not cover exactly the same A_V and $(m-M)_0$ intervals. In any case, the relative minima are well delimited in all cases, as illustrated in Fig. 8. The $[\text{Fe}/\text{H}]$ spacing between these maps is of $\Delta[\text{Fe}/\text{H}] = 0.07$ dex.

Among these many SFH-recovery experiments, the most interesting ones are obviously those with the relative minima and the absolute minimum χ_{\min}^2 values. Fig. 6 shows the χ^2 and residuals in the Hess diagram for the best fitting solution, which is for $(m-M)_0 = 18.83$, $A_V = 0.345$ and $[\text{Fe}/\text{H}] = -0.88$ and $\chi_{\min}^2 = 0.933$. It is already evident, in this plot, that the fitted solution is an excellent representation of the observed data, with residuals uniformly distributed over the CMD. The only point of the CMD in which there seems to be some increased residual is the bottom part of the main sequence, where according to Figs. 2 and 3, the completeness is significantly smaller than 1 (although by just 10 to 20 %), and photometric errors are higher.

Figure 7 shows two examples of recovered $\text{SFR}(t)$ for best-fitting solutions obtained for different values of $[\text{Fe}/\text{H}]$. They are qualitatively similar, with a clear presence of stars spanning ages from ~ 1.2 Gyr ($\log(t/\text{yr}) = 9.08$) to ~ 1.9 Gyr ($\log(t/\text{yr}) = 9.28$).

3.2 Evaluating the errors

To evaluate the errors for all involved parameters the first step was to find the correspondence between the χ_{\min}^2 value for each model and its significance (or confidence) level, α . This correspondence was estimated simulating 100 synthetic CMDs generated with a number of stars equal to the observed CMD, using the best-fitting $\text{SFR}(t)$ and its parameters as the input for the simulations. So, after recovering the SFH for this sample of synthetic CMDs, it was possible to build the χ_{\min}^2 distribution and to establish the relation between the χ_{\min}^2 difference above the minimum and α .

Figure 8 shows the significance levels for all the solutions depicted in Fig. 5. As one sees, for all $[\text{Fe}/\text{H}]$ between -0.74 and -0.95 there are ample areas of the A_V versus $(m-M)_0$ diagrams with solutions within the 95 % significance level. The best solutions, with χ_{\min}^2 close to 0.95 and significance levels of about 30 %, are limited to the central regions of the $[\text{Fe}/\text{H}] = -0.81$, -0.88 , and -0.95 diagrams.

These maps can be used to estimate the mean values of the parameters that characterize the best-fitting solutions, and their errors. These are determined as the mean and standard deviation, weighted by $1-\alpha$, inside the regions in which $\alpha < 0.68$. The results are:

$$\begin{aligned} (m-M)_0 &= 18.84 \pm 0.04 \\ A_V &= 0.33 \pm 0.05 \\ [\text{Fe}/\text{H}] &= -0.86 \pm 0.09 \end{aligned}$$

These numbers give an idea of the region of parameter space actually covered by the best-fitting solutions.

Fig. 9 presents the $\text{SFR}(t)$ for the overall best fitting

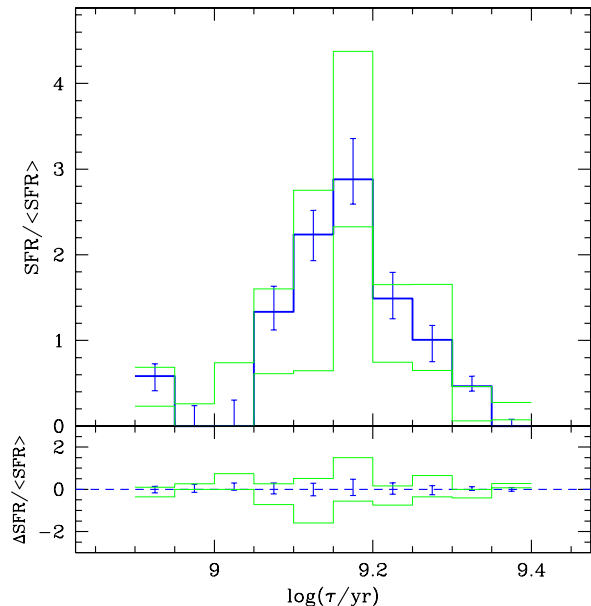


Figure 9. The overall best-fitting solution for the $\text{SFR}(t)$ of NGC 419. The random (error bars) and systematic errors (solid thin lines) are also shown.

solution, obtained at $[\text{Fe}/\text{H}] = -0.88$, and corresponding to the Hess diagrams of Fig. 6. Overplotted on the $\text{SFR}(t)$, we have the random errors due to the statistical fluctuations (associated to the number of stars); they were determined from the r.m.s. dispersion in the recovered $\text{SFR}(t)$ for the 100 synthetic CMDs. On the other hand, the systematic errors in the $\text{SFR}(t)$ due to the uncertainties in $(m-M)_0$, A_V and $[\text{Fe}/\text{H}]$, were determined using the minimum and maximum $\text{SFR}(t)$ values for all models inside the 68 % significance level for all metallicities.

3.3 The role of the binary fraction

As anticipated previously, we have verified that the binary fraction f_b plays a relatively minor role in determining the best-fitting solution and the $\text{SFR}(t)$. Many simulations at varying f_b were tried at several stages of our analysis, always supporting this conclusion, and always pointing to a binary fraction close to 0.2. Fig. 10 aims to illustrate the sort of results one gets for different f_b . To build the figure, we first define a large set of SFH-solutions for which the CMD fitting was considered to be good: namely the entire 68 % significance level area for the metallicity $[\text{Fe}/\text{H}] = -0.81$, in Fig. 8. For this region of the A_V versus $(m-M)_0$ plane, the SFH-recovery tests are repeated for all f_b values between 0.10 and 0.28, at steps of 0.02. Then, we plot the value of mean χ_{\min}^2 and its r.m.s. dispersion as a function of f_b , as shown in Fig. 10. The minimum of mean χ_{\min}^2 for $f_b = 0.18$ is evident. However, the dispersion of χ_{\min}^2 values is also significant, and indicates that a relatively wide range of f_b , from say 0.12 to 0.24, would also produce acceptable results, if compared to the $f_b = 0.18$ case.

It is also worth noticing that for $f_b = 0.18$ the 68 % significance level ($\alpha = 0.68$) is about 0.038 above the minimum χ_{\min}^2 , as determined in the previous section. All solu-

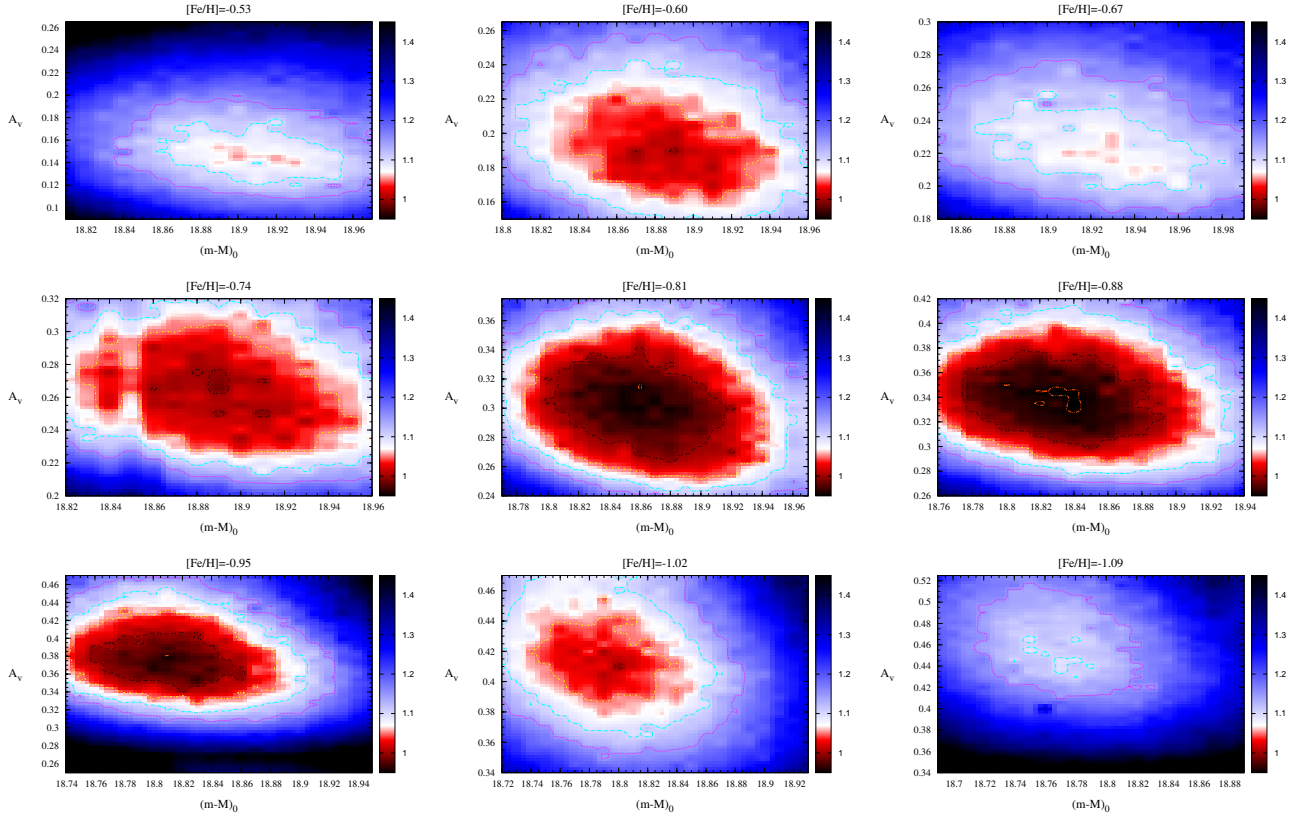


Figure 5. Maps of the χ_{\min}^2 obtained during SFH-recovery, χ_{\min}^2 , as a function of $(m-M)_0$ and A_V , for several $[\text{Fe}/\text{H}]$ values.

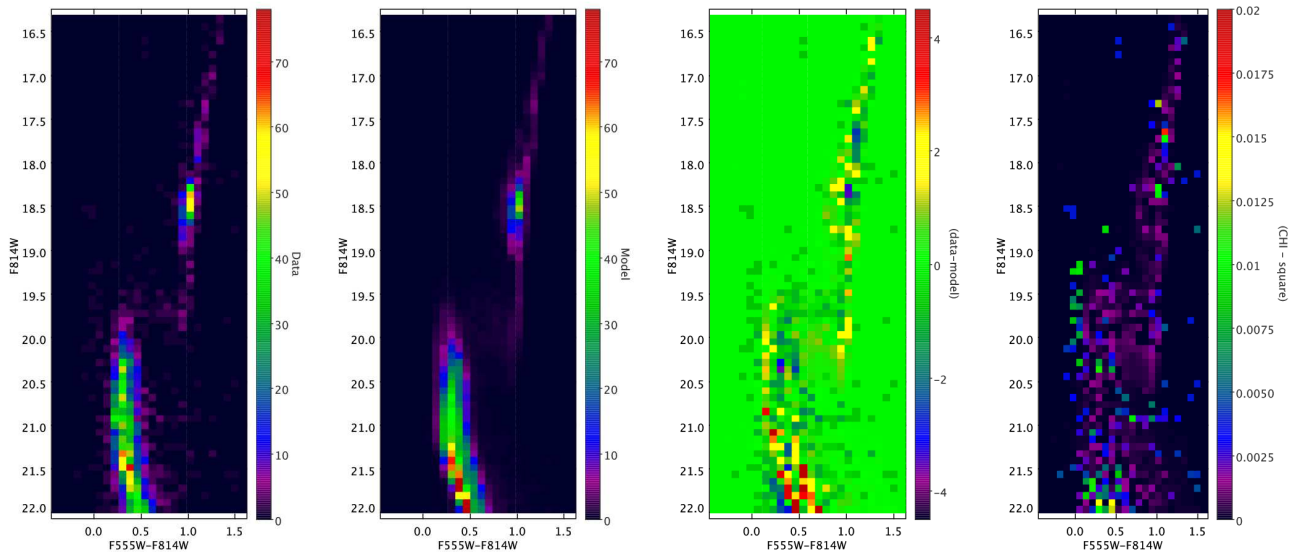


Figure 6. In the Hess diagram, we show the data (left), the solution found by StarFISH (middle), the data-model difference and the χ^2 map. The model is for $[\text{Fe}/\text{H}] = -0.88$, $(m-M) = 18.83$, $A_V = 0.345$, $f_b = 0.18$.

tions presented in Fig. 10 are inside this limit. So, even if there is a apparent minimum χ_{\min}^2 around $f_b = 0.18$, it is not statistically significant.

Finally, Fig. 11 shows the recovered $\text{SFR}(t)$ for four different f_b values over the $f_b = 0.12$ to 0.28 interval. Not only the $\text{SFR}(t)$ is seen to vary by amounts that are comparable

to the random errors in Fig. 9, but they also do it in a non-systematic way: the mean age and shape of the $\text{SFR}(t)$ do not show any significant trend with f_b .

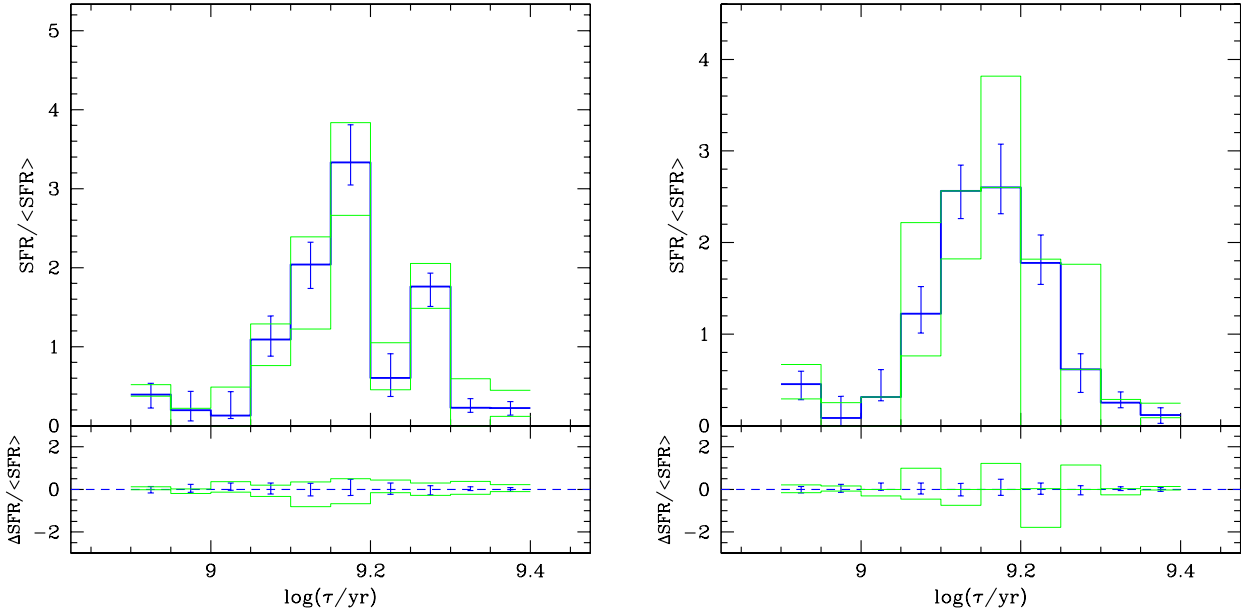


Figure 7. The $SFR(t)$ corresponding to the best fitting solution (blue histogram), for metallicities $[Fe/H] = -0.95$ (left) and -0.81 (right). The error bars indicate the random errors, whereas the green histograms indicate the systematic errors (see Sect. 3.2 for more details).

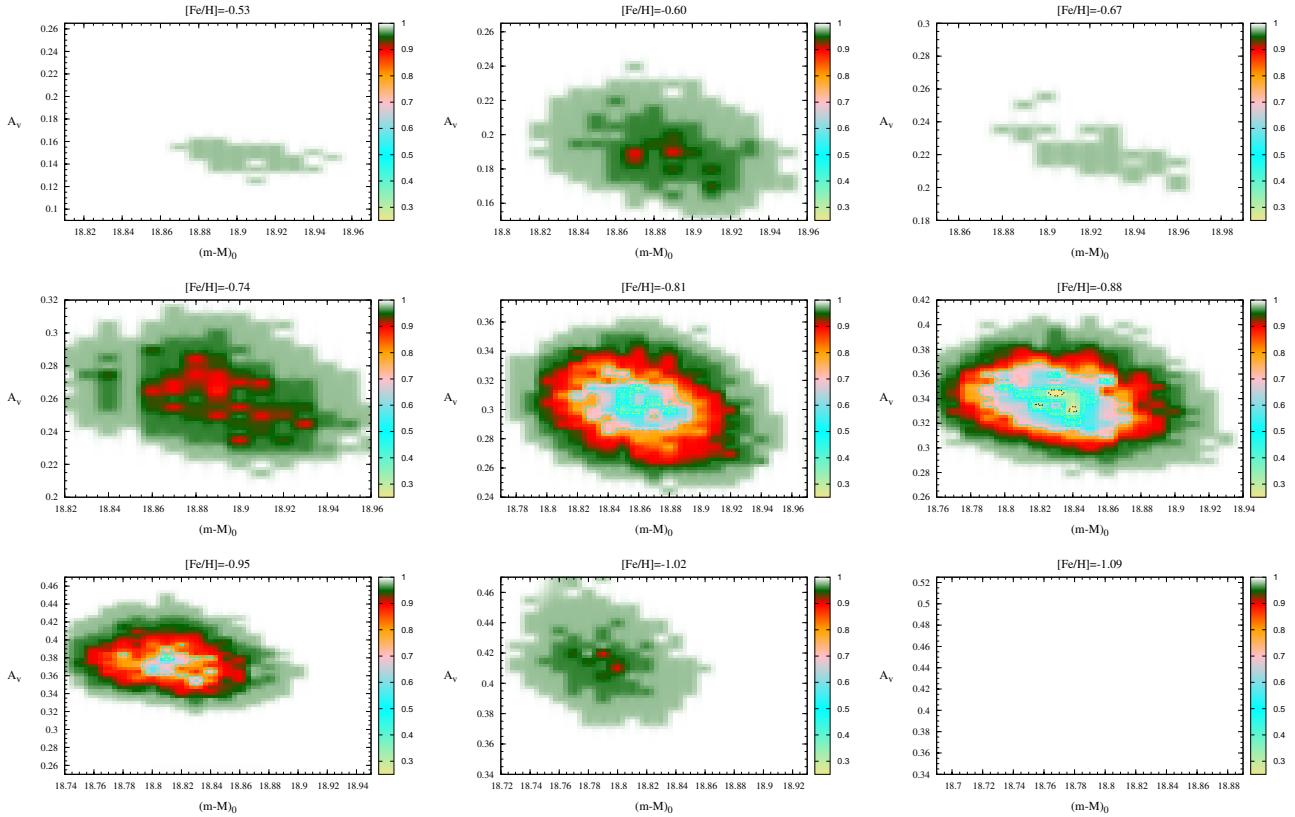


Figure 8. Significance level distributions for several $[Fe/H]$ values.

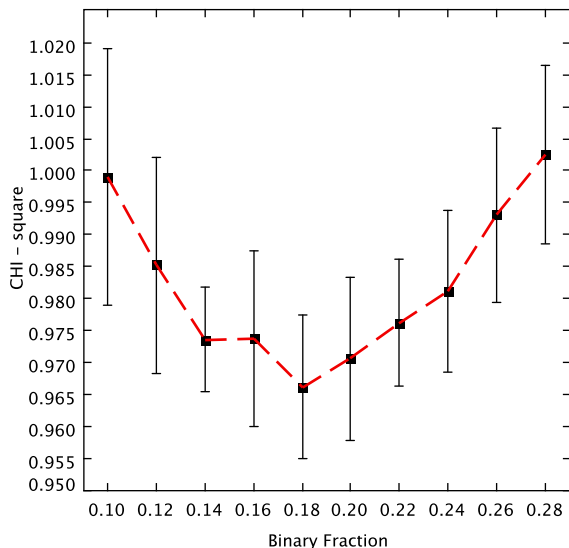


Figure 10. The average of the minimum χ_{\min}^2 versus the binary fraction f_b , for a series of models of metallicity $[\text{Fe}/\text{H}] = -0.81$.

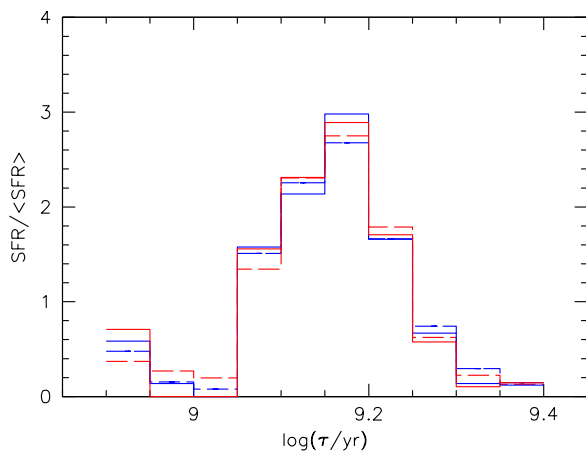


Figure 11. The $\text{SFR}(t)$ for a series of SFH solutions with $[\text{Fe}/\text{H}] = -0.81$, $(m-M)_0 = 18.86$, $A_V = 0.315$, and for different binary fractions: $f_b = 0.12$ (blue dashed line), 0.18 (red dashed), 0.24 (blue solid), and 0.28 (red solid).

3.4 The role of the field contamination

In this work, we have analysed the ACS/HRC photometry NGC 419 without taking into account that a fraction of the observed stars is due to the SMC field. Indeed, when first noticing the unusual structure of the red clump in these data, Glatt et al. (2008) suggested the fainter red clump could be due to the SMC field. The counter-argument by Girardi et al. (2009a), however, has dramatically re-dimensioned the possible role of the SMC field contamination in this case: after measuring the density of red clump stars in the external parts of the ACS/WFC images of the same cluster, at radii larger than $75''$ and for a total area of $2.47 \times 10^4 \text{ arcsec}^2$, they find that just 4.5 red clump stars from the SMC field are expected to be found inside the

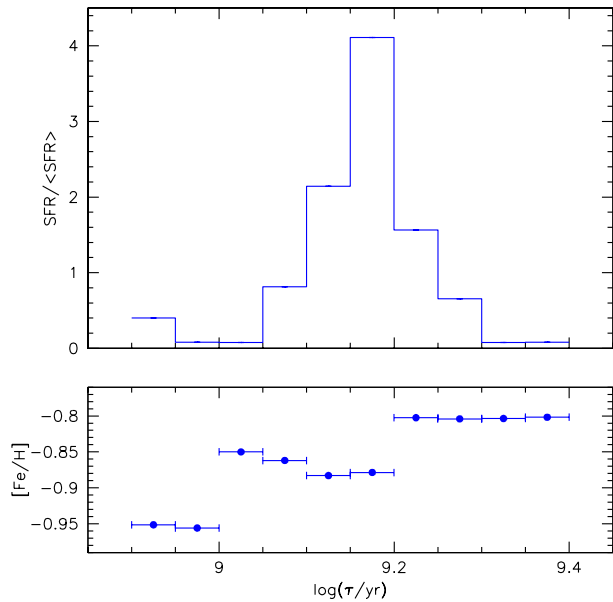


Figure 12. The $\text{SFR}(t)$ and AMR obtained when the $[\text{Fe}/\text{H}]$ is not constrained to a single value, but is let to vary between 4 different values in the $-0.95 \leq [\text{Fe}/\text{H}] \leq -0.80$ interval. The upper panel shows the $[\text{Fe}/\text{H}]$ -added $\text{SFR}(t)$, whereas the bottom panel show the SFR -averaged $[\text{Fe}/\text{H}](t)$.

740 arcsec^2 area of the HRC images, whereas the total observed number is of 388 (47 of them are in the secondary clump). These numbers set the probability that the secondary clump in NGC 419 is made of SMC field stars to less than 10^{-9} (Girardi et al. 2009b). Moreover, they indicate that the field contamination in the red clump area of the CMD is of just $\sim 1\%$.

In the context of the SFH-recovery work, some additional numbers worth of consideration are the following. The number of field main sequence stars in the magnitude interval $20 < F814W < 22$, for the same $2.47 \times 10^4 \text{ arcsec}^2$ area in the outskirts of the WFC images, is 2640, whereas the observed number in the 740 arcsec^2 of HRC is 2395. This magnitude interval is just barely affected by incompleteness, and contains most of the observed stars. Therefore, we can estimate that just $\sim 3.3\%$ of the stars used to study the SFH of NGC 419 are due to the SMC field. This fraction is similar to the Poisson noise in the total number of HRC stars, indicating that our SFH results cannot be affected in a significant way.

3.5 The age-metallicity relation

With star formation lasting for 700 Myr, one may wonder whether NGC 419 would not have enriched itself with metals ejected from its oldest stellar populations. Although we believe that the present photometric data is not enough to clarify this question, we performed an additional SFH-recovery exercise, in which the cluster $[\text{Fe}/\text{H}]$ is not fixed, but can take four different values at each age: $[\text{Fe}/\text{H}] = -0.95, -0.90, -0.85, -0.80$. In practice, this is obtained by running the SFH-recovery method with a larger library of partial models, with 40 components (10 age bins times 4 metallicity bins).

This larger set of partial models provides more freedom to the StarFISH algorithm, which converges to an absolute best-fitting solution with a χ^2_{\min} of just 0.84, for $A_V = 0.33$ and $(m-M)_0 = 18.83$. The SFH results are illustrated in Fig. 12: the upper panel shows the $\text{SFR}(t)$ obtained by adding the SFR values obtained for all metallicities at each age bin, whereas the bottom panel shows the AMR as obtained by a SFR-weighted average of the four different $[\text{Fe}/\text{H}]$ values.

This $\text{SFR}(t)$ is actually very similar to the one obtained from the best-fitting solution with $[\text{Fe}/\text{H}] = -0.88$ (Fig. 9). In the age interval with significant star formation, which goes from 1.2 to 1.9 Gyr and comprises 5 age bins, the three youngest age bins are found to have a metallicity almost coincident with the $[\text{Fe}/\text{H}] = -0.88$ one, whereas the two oldest ones are found to be slightly more metal-rich, with -0.80 dex. It is not clear whether this $[\text{Fe}/\text{H}]$ variation can be significant, since it is comparable to the estimated error of 0.09 dex in the $[\text{Fe}/\text{H}]$ of the best-fitting solutions (Sect. 3.2). We conclude that our analysis does not provide evidence for self-enrichment taking place in NGC 419.

4 CONCLUSIONS

In this paper, we have derived the SFH of the SMC star cluster NGC 419, via the classical method of CMD reconstruction. This analysis implicitly assumes that NGC 419 is formed by a sum of single-burst stellar populations (or “partial models”), each one being characterized by a well-defined and narrow MSTO. The only effects that blur these partial models in the CMDs are the sequences of binaries (which effect however is far from dramatic) and the photometric errors. With this kind of approach, the broad MMSTO observed in NGC 419 naturally translate into a continued star formation history. We find a $\text{SFR}(t)$ lasting for 700 Myr (from 1.2 to 1.9 Gyr, see Fig. 9), which is quite a long period, probably at the upper limit of all values already estimated for star clusters with MMSTOs (Bertelli et al. 2003; Baume et al. 2007; Mackey & Broby Nielsen 2007; Mackey et al. 2008; Milone et al. 2009; Goudfrooij et al. 2009). Our error analysis leaves practically no room for the MMSTOs in this cluster being caused by a single episode of star formation.

It is also remarkable that the $\text{SFR}(t)$ we derive presents a pronounced maximum at the middle of the star formation interval, at an age of 1.5 Gyr (Fig. 9). This is somewhat unexpected, in the context of the few suggested scenarios for the appearance of prolonged star formation in LMC star clusters (see Goudfrooij et al. 2009, for a comprehensive discussion of them). Either the merging of two star clusters (Mackey & Broby Nielsen 2007), or a second period of star formation driven by the merging with a giant molecular cloud (Bekki & Mackey 2009), would lead to strongly bimodal distributions of cluster ages, which we do not find in NGC 419. Only in the case of the best model with $[\text{Fe}/\text{H}] = -0.95$, there is an indication of two different peaks in the $\text{SFR}(t)$ (see Fig. 7), which however are neither separated nor followed by periods of null $\text{SFR}(t)$. Also the trapping of field stars by the forming star cluster (Pflamm-Altenburg & Kroupa 2007) would lead to different results, with the major peak of star formation being found at

the youngest ages. On the other hand, our findings seem to be more in line with Goudfrooij et al. (2009)’s conclusions, based on the quite continuous distribution of stars across the MMSTO region of the LMC cluster NGC 1846. They suggest a scenario in which the star cluster continues to form stars in its center out of the ejecta of stars from previous generations. In our case, however, this process would have to proceed for a significantly more extended period of time than for NGC 1846, and peak – somewhat against the most naive expectations – at the middle of the star formation period. Also, this latter scenario might imply some amount of self-enrichment in this cluster, whereas our method instead is compatible either with a constant metallicity, or with some amount of metal dilution. Needless to say, the present observational data is not clear enough to provide unambiguous indications about the formation scenario of such clusters.

Another basic result of our analysis is that the hypothesis of continued SFH, together with current stellar evolutionary models and a modest fraction of binaries, produces *excellent fits to the CMD of NGC 419*, with χ^2_{\min} as small as 0.93 – or even 0.84 if the $[\text{Fe}/\text{H}]$ is let to vary during the SFH-recovery. We have translated this result into quantitative estimates for the random and systematic errors of the derived $\text{SFR}(t)$. It is obvious that many combinations of cluster parameters produce acceptable solutions, with significance levels smaller than 95 %. However, the really good solutions – i.e. those with significance levels better than 68 % – cover a narrow region of the parameter space, comprising less than 0.1 mag in both $(m-M)_0$ and A_V , and about 0.1 dex in $[\text{Fe}/\text{H}]$.

Despite our success in fitting the CMD of NGC 419 as a sum of partial models, this success does not tell us about the reliability of alternative hypotheses for the origin of MMSTOs. In particular, we cannot conclude anything about Bastian & de Mink (2009)’s hypothesis based on the colour spread of coeval stars with different rotation rates, since its capability of providing a *quantitative* description of the data has not yet been tested. We urge that this test should be performed, in order to shed light into this problem.

However, we call attention to another question that has to be properly addressed: Is Bastian & de Mink (2009)’s rotation hypothesis able to produce, in addition to the broad turn-off of Magellanic Cloud star clusters, also the dual red clump observed in NGC 419 (see Girardi et al. 2009a)? In our models with prolonged star formation, the 700 Myr spread in age translates into a $\sim 0.26 M_{\odot}$ spread in turn-off masses, which in turn implies a small spread in the mass of H-exhausted cores as stars leave the main sequence. This small spread – of the order of just $\sim 0.01 M_{\odot}$ – is enough to cause the appearance of a dual red clump in this cluster, as thoroughly discussed in Girardi et al. (2009a,b). Such a feature is then *naturally present* in our best-fitting solutions, as can be appreciated in Fig. 6. Can rotation do the same, producing spreads of a compatible magnitude both in the main sequence and in the red clump? Moreover, can this be achieved with a reasonable and simple enough distribution of rotation velocities? At first sight, this seems very unlikely to us.

ACKNOWLEDGMENTS

We thank the anonymous referee for the useful suggestions. The data presented in this paper were obtained from the Multimission Archive at the Space Telescope Science Institute (MAST). STScI is operated by the Association of Universities for Research in Astronomy, Inc., under NASA contract NAS5-26555. We thank the support from INAF/PRIN07 CRA 1.06.10.03, contract ASI-INAF I/016/07/0, and the Brazilian agencies CNPq and FAPESP.

REFERENCES

- Bastian N., de Mink S. E., 2009, *MNRAS*, 398, L11
- Baume G., Carraro G., Costa E., Méndez R. A., Girardi L., 2007, *MNRAS*, 375, 1077
- Bekki K., Mackey A. D., 2009, *MNRAS*, 394, 124
- Bertelli G., Nasi E., Girardi L., Chiosi C., Zoccali M., Gallart C., 2003, *AJ*, 125, 770
- Chabrier G., 2001, *ApJ*, 554, 1274
- Cioni M., Bekki K., Clementini G., de Blok W. J. G., Emerson e. a., 2008, *Publications of the Astronomical Society of Australia*, 25, 121
- Crowl H. H., Sarajedini A., Piatti A. E., Geisler D., Bica E., Clariá J. J., Santos Jr. J. F. C., 2001, *AJ*, 122, 220
- Dolphin A. E., 2002, *MNRAS*, 332, 91
- Dolphin A. E., Saha A., Skillman E. D., Dohm-Palmer R. C., Tolstoy E., Cole A. A., Gallagher J. S., Hoessel J. G., Mateo M., 2003, *AJ*, 126, 187
- Durand D., Hardy E., Melnick J., 1984, *ApJ*, 283, 552
- Elson R. A. W., Sigurdsson S., Davies M., Hurley J., Gilmore G., 1998, *MNRAS*, 300, 857
- Gallagher J. S., Mould J. R., de Feijter E., Holtzman J., Stappers e. a., 1996, *ApJ*, 466, 732
- Gallart C., Freedman W. L., Aparicio A., Bertelli G., Chiosi C., 1999, *AJ*, 118, 2245
- Girardi L., Dalcanton J., Williams B., de Jong R., Gallart C., Monelli M., Groenewegen M. A. T., Holtzman J. A., Olsen K. A. G., Seth A. C., Weisz D. R., the ANGST/ANGRRR Collaboration 2008, *PASP*, 120, 583
- Girardi L., Groenewegen M. A. T., Hatziminaoglou E., da Costa L., 2005, *A&A*, 436, 895
- Girardi L., Rubele S., Kerber L., 2009a, *MNRAS*, 394, L74
- Girardi L., Rubele S., Kerber L., 2009b, preprint (arXiv:0910.3139)
- Glatt K., Grebel E. K., Gallagher J. S., Nota A., Sabbi E., Sirianni M., Clementini G., Da Costa G., Tosi M., Harbeck D., Koch A., Kayser A., 2009, *AJ*, 138, 1403
- Glatt K., Grebel E. K., Sabbi E., Gallagher J. S., Nota A., Sirianni M., Clementini G., Tosi M., Harbeck D., Koch A., Kayser A., Da Costa G., 2008, *AJ*, 136, 1703
- Goudfrooij P., Puzia T. H., Kozhurina-Platais V., Chandar R., 2009, *AJ*, 137, 4988
- Gouliermis D., Keller S. C., Kontizas M., Kontizas E., Bellas-Velidis I., 2004, *A&A*, 416, 137
- Harries T. J., Hilditch R. W., Howarth I. D., 2003, *MNRAS*, 339, 157
- Harris J., Zaritsky D., 2001, *ApJS*, 136, 25
- Harris J., Zaritsky D., 2004, *AJ*, 127, 1531
- Kayser A., Grebel E. K., Harbeck D. R., Cole A. A., Koch A., Gallagher J. S., da Costa G. S., 2009, *The Age-Metallicity Relation of the SMC*. pp 157–+
- Kerber L. O., Girardi L., Rubele S., Cioni M.-R., 2009, *A&A*, 499, 697
- Kerber L. O., Santiago B. X., Brocato E., 2007, *A&A*, 462, 139
- Lah P., Kiss L. L., Bedding T. R., 2005, *MNRAS*, 359, L42
- Mackey A. D., Broby Nielsen P., 2007, *MNRAS*, 379, 151
- Mackey A. D., Broby Nielsen P., Ferguson A. M. N., Richardson J. C., 2008, *ApJ*, 681, L17
- Marigo P., Girardi L., Bressan A., Groenewegen M. A. T., Silva L., Granato G. L., 2008, *A&A*, 482, 883
- Mighell K. J., Rich R. M., Shara M., Fall S. M., 1996, *AJ*, 111, 2314
- Milone A. P., Bedin L. R., Piotto G., Anderson J., 2009, *A&A*, 497, 755
- Mucciarelli A., Carretta E., Origlia L., Ferraro F. R., 2008, *AJ*, 136, 375
- North P. L., Gauderon R., Royer F., 2009, in J. T. van Loon & J. M. Oliveira ed., *IAU Symposium Vol. 256 of IAU Symposium*, New distance and depth estimates from observations of eclipsing binaries in the SMC. pp 57–62
- Parisi M. C., Grocholski A. J., Geisler D., Sarajedini A., Clariá J. J., 2009, *AJ*, 138, 517
- Pflamm-Altenburg J., Kroupa P., 2007, *MNRAS*, 375, 855
- Rich R. M., Shara M., Fall S. M., Zurek D., 2000, *AJ*, 119, 197
- Rich R. M., Shara M. M., Zurek D., 2001, *AJ*, 122, 842
- Schlegel D. J., Finkbeiner D. P., Davis M., 1998, *ApJ*, 500, 525
- Sirianni M., Jee M. J., Benítez N., Blakeslee J. P., Martel A. R., Meurer G., Clampin M., De Marchi G., Ford H. C., Gilliland R., Hartig G. F., Illingworth G. D., Mack J., McCann W. J., 2005, *PASP*, 117, 1049
- Stetson P. B., 1987, *PASP*, 99, 191
- Zaritsky D., Harris J., Thompson I. B., Grebel E. K., Massey P., 2002, *AJ*, 123, 855